

# Cookoff of Powdered and Pressed Explosives Using a Micromechanics Pressurization Model

Michael L. Hobbs,<sup>\*,[a]</sup> Judith A. Brown,<sup>[a]</sup> Michael J. Kaneshige,<sup>[a]</sup> and Cuauhtemoc Aviles-Ramos<sup>[b]</sup>

**Abstract:** Cookoff experiments of powdered and pressed TATB-based plastic bonded explosives (PBXs) have been modeled using a pressure-dependent universal cookoff model (UCM) in combination with a micromechanics pressurization (MMP) model described in a companion paper. The MMP model is based on the accumulation of decomposition gases at nucleation sites that load the surrounding TATB crystals and binder. This is the first cookoff model to use an analytical mechanics solution for compressibility and thermal expansion to describe internal pressurization caused by both temperature and decomposition occurring

within closed-pore explosives. This approach produces more accurate predictions of ignition time and pressurization within high-density explosives than simple equation-of-state models. The current paper gives details of the reaction chemistry, model parameters, predicted uncertainty, and validation using experiments from multiple laboratories with errors less than 6%. The UCM/MMP model framework gives more accurate thermal ignition predictions for high density explosives that are initially impermeable to decomposition gases.

**Keywords:** Micromechanics • Pressurization • Cookoff • Thermal Ignition • TATB

## 1 Introduction

The current paper is an application of a micromechanics pressurization (MMP) model that is based on pore nucleation and growth described in a companion paper [1] with application to cookoff of explosives. The model describes explosives that thermally ignite after being exposed to high temperatures such as fire. In this work, pores are assumed to be located at nucleation sites with pore radii increasing as decomposition gases accumulate within pores. The pore radii are also displaced mechanically via thermal expansion as well as differences in internal and external pore pressures.

A maximum pore pressure is used to differentiate between pores that are open and pores that are closed. The maximum pore pressure is based on extrapolation of compressive strength to cookoff temperatures between 525 and 575 K as discussed further in the companion paper [1]. Gases can migrate between open pores and can fill external gas ullage. However, gases cannot move between pores that are closed. Thus, the MMP model describes dynamic damage evolution as the explosive changes from impermeable layers to gas permeable layers.

The MMP model is an analytical solution for pressurization caused by thermal decomposition and mechanical displacements. Temperature and the decomposition dependent solid fraction can either be supplied directly to the MMP model or can be determined using a thermal/chemical solver. In the current paper, the MMP model is solved simultaneously with the energy equation and a decomposition mechanism. Temperature is obtained by solving

the conductive energy equation with a volumetric energy source associated with chemical decomposition. The decomposition mechanism in the current work is based on a universal cookoff model [2] for explosives. The BKW-EOS is used for the gas-phase equation of state [1].

The explosive described in the current work is an insensitive high explosive (IHE) composed of 95 wt.% of the IHE triaminotrinitrobenzene (TATB) and 5 wt.% chlorotri-fluoroethylene/vinylidene fluoride binder (Kel-F). Safety concerns arise since thermally degraded IHE is more sensitive to shock than room temperature IHE [3]. In fact, thermally degraded PBXs containing TATB heated to 252 °C and held for 20 min had similar shock sensitivity to room temperature PBXs containing HMX [4,5] (e.g. 95 wt.% octahydro-1,3,4,7-tetranitro-1,3,5,7-tetrazocine or HMX with a 5 wt.% binder). The increased sensitivity has been attributed to elevated hot spot temperatures [4]. A few of the TATB experiments were thermally cycled to determine the effects of ratchet growth which is beyond the scope of the present work. However, the MMP model can predict damage such as the evolution of specific surface area which is useful for safety analysis involving explosives in accidental fires.

[a] M. L. Hobbs, J. A. Brown, M. J. Kaneshige  
Sandia National Laboratories  
P.O. Box 5800, Albuquerque, NM 87185, USA  
\*e-mail: mlhobbs@sandia.gov

[b] C. Aviles-Ramos  
Los Alamos National Laboratory  
P.O. Box 1663, Los Alamos, NM 87545, USA

Tarver et al. [6,7] presented several global three-step reaction mechanisms to model cookoff of TATB using one-dimensional time-to-explosion (ODTX) data. Tarver concluded that gas-phase reactions do not dominate energy release since confined and unconfined ODTX data give similar explosion times. Tarver's observation was for high-density explosives where the decomposition gases may have been retained within the explosive as implied by the work of Englert-Erickson et al. [8]. In contrast, we measured large differences in explosion times between sealed and vented cookoff of TATB in the Sandia Instrumented Thermal Ignition (SITI) experiment [9]. For example, the thermal ignition times for vented (7509 s) and sealed (3041 s) experiments using low-density molding powders exposed to the same boundary temperatures of 573.5 K were significantly different.

Thermal ignition time or time-to-ignition is defined as the time delay between exposure of the external boundary of the explosive or confinement to high temperatures and the time when the apparatus containing the explosive disassembles due to an exothermic runaway reaction. Time-to-ignition is sometimes referred to as time-to-explosion. Cookoff is the unintentional failure of a reactive material exposed to high temperatures. The current work focuses on the state of the explosive from room temperature to thermal ignition which is typically a slow process. Dynamic processes leading to cookoff violence are beyond the scope of the present work.

We previously modeled cookoff of TATB-based explosives using a four-step mechanism with one of the steps accelerated by pressure [9], which was later validated using larger-scale experiments [10]. Similarly, Moore et al. [11] described decomposing TATB using a reaction rate accelerated by gaseous decomposition products. These two models [9,11] support the hypothesis that the decomposition of TATB depends on both the gas composition and concentration. This hypothesis is tested in the current work by simulating sealed and vented thermal ignition of TATB with a pressure-dependent universal cookoff model [2] coupled to a micromechanics pressurization model [1].

Englert-Erickson et al. [8] concluded that TATB-based PBXs are impermeable until just prior to thermal ignition where internal pressure produces macro-scale cracking. We have also observed decomposition gases creating porosity in our high-density SITI experiments as shown in Figure 1. Figure 1(a) shows a pristine pressed 2.54 diameter cylinder of PBX used in our SITI cookoff experiments that can be compared to the thermally damaged PBX shown in Figure 1(b) and (c).

Figures 1(b) and (c) show post-ignition pictures of the SITI runs 13 (249s25) and 24 (271s50), which had air-filled ullages that were 25% and 50% of the total confined volume. The increase in explosive volume is close to the ullage volumes for each of these experiments. We hypothesize that porosity develops prior to thermal ignition especially when the air-filled ullage is large allowing additional volu-

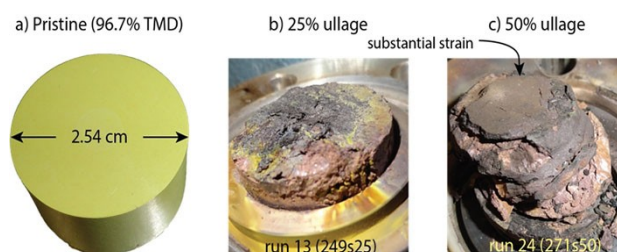


**Figure 1.** Pictures of (a) pristine and (b, c) thermally damaged TATB-based PBX. The pristine PBX was initially confined by aluminum with (b) 25% and (c) 50% of the overall volume being gas-filled ullage. The exterior temperature of the aluminum confinement was ramped from room temperature to set point temperatures of (b) 538.5 K and (c) 533.5 K and held until the PBX thermally ignited and then quenched. The pictures in (b) and (c) were obtained after the PBX had cooled down. The amount of swelling is significantly different for the two ullage volumes.

metric thermal strain. This porosity can either be connected (permeable) or not connected (impermeable) to the ullage where the pressure is measured.

One objective of the current work is to determine whether TATB-based PBXs at densities near the theoretical maximum density (TMD, 1942 kg/m<sup>3</sup>) are permeable prior to thermal ignition. We have performed both experiments and modeling at various conditions to support this hypothesis. In the current work, permeable refers to a material that allows gas to readily pass through. Impermeable refers to a material that does not allow gas to pass through it. Permeability is a material property that describes the ability of a porous material to allow gases to pass through, which is related to the porosity, but also to the geometry of the pores. More information on permeability can be found in Erikson et al. [12].

Typical measured pressures in our SITI apparatus increase monotonically. However, periodically the SITI apparatus leaks and the measured ullage pressure decreases. These leaks can reseal and cause measured ullage pressure to increase. Abrupt increases in measured pressure have also been observed where material damage results in release of decomposition gases into the ullage. These observations support our hypothesis that gases are retained within an impermeable explosive that periodically fails, causing abrupt increases in measured pressures that also cause the apparatus to fail or leak. These scenarios are addressed by using a micromechanical pressurization model limited by the available confinement volume.

The remainder of the paper describes experiments and models of both low-density and high-density PBXs containing TATB. Sealed, vented, and open experiments are used to show various types of thermal damage, such as swelling and surface flaking. This damage is observed using video images of the open experiments and borescope images of the confined experiments. Details of the thermal/chemistry model (UCM) with parameters for the PBX are also dis-

cussed. The coupled thermal/chemistry model (UCM) combined with the micromechanics pressurization (MMP) model is referred to as the UCM/MMP model. The coupled UCM/MMP model is validated using pressed PBX experiments from various laboratories. These experimental and modeling results are used to support the hypothesis that the explosive becomes permeable during decomposition as the explosive swells into the available ullage space.

## 2 Experiments

The Sandia Instrumented Thermal Ignition (SITI) experiment has been used to measure thermal ignition in a variety of explosives such as AN (ammonium nitrate) [13], TNT (trinitrotoluene) [14], PETN (pentaerythritol tetranitrate) [15], HMX (octahydro-1,3,5,7-tetranitro-1,3,5,7-tetrazonine) based explosives [16,17], RDX (hexahydro-1,3,5-trinitro-1,3,5-triazine) based explosives [18], Comp-B (60:40 RDX:TNT) [19],  $\epsilon$ -CL-20 (2,4,6,8,10,12-hexanitro-2,4,6,8,10,12-hexaazaisowurtzitane) [20], black powder and

smokeless powders [21]. We have used many varieties of the SITI experiment with various ullage and explosive volumes. Figures 2(a,d,e, and f) show the SITI configurations used in the current work. Figures 2(b) and (c) show the molding powders and pressed pellets composed of TATB-based PBXs, respectively. Gases accumulating between the molding powder prills are permeable to decomposition gases. However, gases within crystals may not be permeable until a failure pressure has been exceeded. Tables 1 and 2 give details of the molding powder and pressed pellet experiments, respectively. Ignition times are shown in Figure 3.

Figure 2(b) shows nine thermocouples located at the center of the low-density SITI experiments. Similarly, the high-density SITI experiments have an array of nine thermocouples placed between two pressed 2.54 cm diameter by 1.27 cm high cylinders of explosive at various radial distances, which are listed in Figure 2(b). Various gas-filled ullage volumes are used in the current work with average diameters of  $2.22 \pm 0.005$  cm. The heights of the expansion volumes vary depending on the total ullage volumes listed

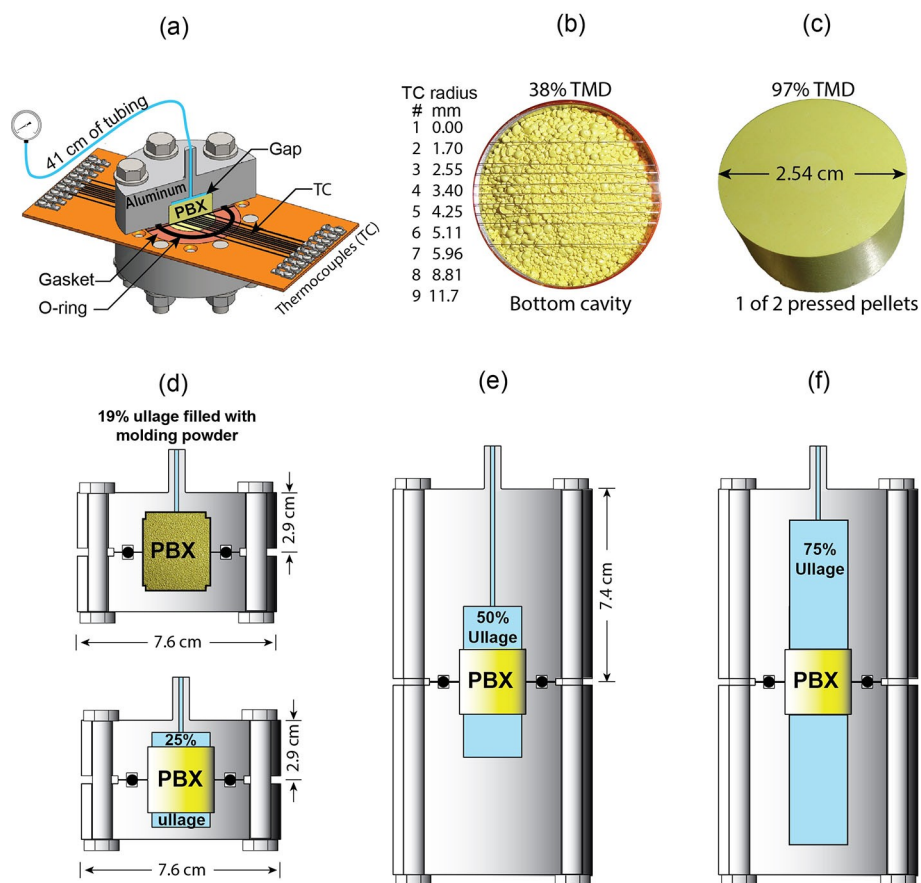


**Figure 2.** (a) SITI schematic and (b) molding powders, and (c) pressed pellets of TATB-based PBXs. The thermocouple (TC) junction radial locations are given in (b). The pressed explosives shown in (c–f) consist of two 2.54 cm diameters by 1.27 cm tall cylinders. One of these cylinders is shown in (c). The ullage for the molding powder experiments was 19% of the overall confinement volume and was filled with prills as shown in (d). The experiments with pressed pellets had (d) 25%, (e) 50%, and (f) 75% air-filled ullage.

**Table 1.** Low-density ( $743 \pm 3 \text{ kg/m}^3$  or 38 % TMD) SITI runs using TATB-based PBXs.<sup>[a]</sup>

Run <sup>[b]</sup>	Date	U% <sup>[c]</sup>	$\rho_{bo}$ <sup>[d]</sup> kg/m <sup>3</sup>	$V_{ullage}$ cm <sup>3</sup>	$V_{tube}$ cm <sup>3</sup>	$V_{ex}$ <sup>[e]</sup> cm <sup>3</sup>	$T_{sp}$ K	$1000/T_{sp}$ K <sup>-1</sup>	$t_{ign}$ s
a (225s19)	10/13/11	18.5	747	2.92	0.1	1.90	573.51	1.7436	3041
b (226s19)	10/17/11	18.8	745	2.97	0.1	1.94	563.50	1.7746	5278
c (223v19)	10/11/11	19.3	740	3.07	0.0	2.00	573.50	1.7437	7509
d (228s19)	11/01/11	19.2	741	3.05	0.1	1.99	553.56	1.8065	9950
e (224v19)	10/12/11	19.2	741	3.05	0.0	1.99	563.51	1.7746	14858
f (141s19)	11/10/09	19.2	741	3.05	0.1	1.99	538.30	1.8577	20798
g (140s19)	10/27/09	18.8	744	2.99	0.1	1.95	533.36	1.8749	26016
h (232v19)	11/16/11	18.7	745	2.96	0.0	1.93	553.53	1.8066	28119

[a] External temperature ramped from a nominal temperature of  $295 \pm 1 \text{ K}$  to  $T_{sp}$  in 600 s and held at the set point temperature. [b] The run numbers in parenthesis represent the internal numbering scheme where s and v refer to sealed and vented, respectively. The trailing two digits represent the nominal ullage percent. The simple run numbers (e.g. a, b, c, etc. for powdered explosives and 1, 2, 3 for pressed explosives) sort the runs by thermal ignition times. [c]  $U = 100V_{o,PBX} / (V_{ullage} + V_{o,PBX})$  where  $V_{o,PBX}$  is  $12.87 \text{ cm}^3$ . [d]  $\rho_{bo} \approx m_{o,PBX} / V_{o,PBX}$ . [e]  $V_{ex}$  is the extra gas volume contained within the ullage. However, for molding powders, the extra gas volume is reduced by the initial solid volume within the ullage. For 1D problems, the extra gas volume is  $V_{ex} = V_{ullage}\phi_o + V_{tube}$ , where the initial gas volume fraction is  $\phi_o \approx 1 - \rho_{bo}/\rho_{co}$ .

**Table 2.** High-density ( $1881 \pm 5 \text{ kg/m}^3$  or 97 % TMD) SITI runs using TATB-based PBXs.<sup>[a]</sup>

Run	Date	U%	$\rho_{bo}$ kg/m <sup>3</sup>	$V_{ullage}$ cm <sup>3</sup>	$V_{tube}$ cm <sup>3</sup>	$V_{ex}$ cm <sup>3</sup>	$T_{sp}$ K	$1000/T_{sp}$ K <sup>-1</sup>	$t_{ign}$ s
1 (264v75)	6/11/12	74.9	1869	38.50	0.0	38.50	553.41	1.8070	2141
2 (170s20)	11/17/10	19.7	1876	3.06	0.1	3.16	568.00	1.7606	2251
3 (269s50)	6/20/12	50.2	1874	12.80	0.2	13.00	563.10	1.7759	2490
4 (252s25)	2/16/12	25.8	1883	4.37	0.1	4.47	563.55	1.7745	2636
5 (277s75)	7/13/12	75.0	1875	38.47	0.2	38.66	563.34	1.7751	3375
6 (260s50)	5/30/12	50.3	1888	12.83	0.2	13.03	553.33	1.8072	4662
7 (280s25)	7/19/12	25.2	1888	4.24	0.1	4.35	553.40	1.8070	4778
8 (261s75)	5/31/12	74.9	1883	38.31	0.2	38.50	553.42	1.8069	4987
9 (255v25)	5/8/12	25.1	1875	4.31	0.0	4.31	553.40	1.8070	5504
10 (251v25)	2/15/12	24.7	1882	4.22	0.0	4.22	563.54	1.7745	7794
11 (365s75)	12/12/13	75.0	1808	38.28	0.2	38.48	553.15	1.8078	8131
12 (249s25)	2/10/12	25.7	1891	4.35	0.1	4.45	538.56	1.8568	10625
13 (279v25)	7/17/12	24.9	1889	4.27	0.0	4.27	563.16	1.7757	10741
14 (164s20)	9/29/10	20.0	1880	3.11	0.1	3.22	538.00	1.8587	11213
15 (273v25)	7/3/12	25.3	1880	4.36	0.0	4.36	538.49	1.8570	11569
16 (262s50)	6/1/12	50.2	1880	12.79	0.2	12.99	538.53	1.8569	12611
17 (250s25)	2/13/12	25.7	1883	4.35	0.1	4.45	533.74	1.8736	13623
18 (282v25)	7/25/12	25.7	1888	4.46	0.0	4.46	553.42	1.8069	13945
19 (263s75)	6/5/12	74.9	1881	38.27	0.2	38.47	538.48	1.8571	14326
20 (172s20)	11/19/10	19.4	1880	3.00	0.1	3.11	533.04	1.8760	16018
21 (271s50)	6/27/12	50.1	1881	12.72	0.2	12.91	533.52	1.8743	18319
22 (275v75)	7/10/12	75.1	1883	38.90	0.0	38.90	553.43	1.8069	20829
23 (268s75)	6/19/12	75.0	1885	38.51	0.2	38.71	533.50	1.8744	25175

[a] External temperature ramped from a nominal temperature of  $295 \pm 2 \text{ K}$  to  $T_{sp}$  in 600 s and held at the set point temperature.

in Table 2. A control thermocouple on the exterior of the 7.62 cm diameter aluminum confinement is used to control rope heaters that ramp the exterior temperature of the aluminum from room temperature to a set point temperature in nominally 600 s. The overall height of each of the two confining aluminum cylinders depends on the ullage volume as shown in Figure 2 and varies between 2.2 cm (19 % ullage) and 7.4 cm (75 % ullage). The gases within the ullage are connected to a Kulite HEM-375-20000 A pressure

transducer using 316 L welded and drawn tubing that is annealed. The tubing is either 40.6 cm or 76.2 cm long with an inside diameter of 0.06 cm giving the interior tube volume of 0.1 or 0.2 cm<sup>3</sup>, respectively.



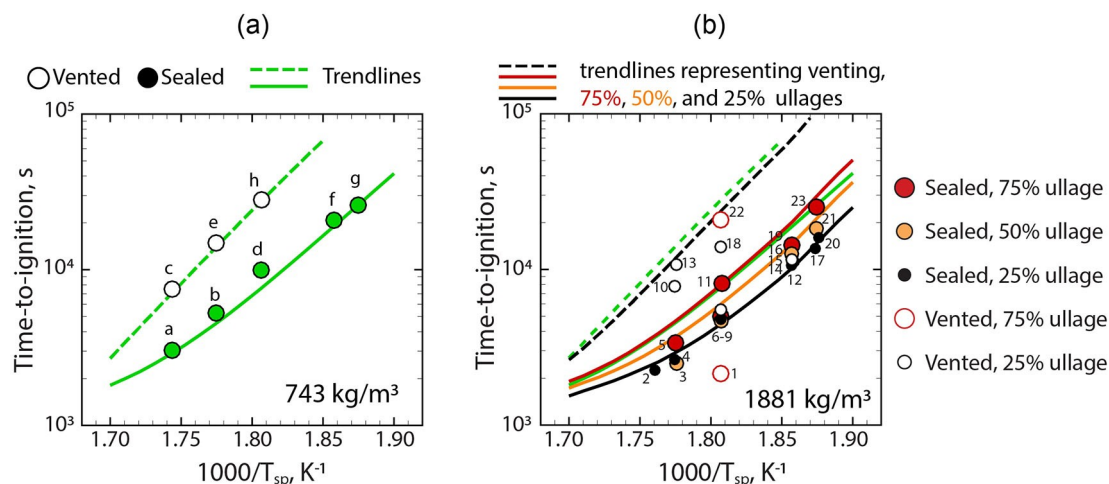


**Figure 3.** Ignition plots for the (a) low-density and (b) high-density runs listed in Tables 1 and 2.

## 2.1 Measured Thermal Ignition Times, Internal Temperatures, and Ullage Pressure

Figures 3(a) and 3(b) show the ignition times for all the PBX runs shown in Table 1 and Table 2, respectively. These times include the ramp time of 600 s as the external temperature is ramped from room temperature (295 K) to the set point temperature. The open and closed symbols represent vented and sealed experiments, respectively. The large, medium, and small sizes of the symbols in Figure 3(b) represent experiments with 75 %, 50 %, and 20–25 % ullage volume, respectively.

Trendlines for both the low-density and high-density experiments are shown in Figure 3(a) and Figure 3(b), respectively. The trendlines were determined based on the model discussed subsequently in Section 3. The dashed green trendline shows that the ignition times are longer for the low-density vented runs than for the high-density vented runs (black dashed line). Faster ignition times in the high-density vented runs, compared to the low-density vented runs, may result from 1) different thermal conductivities or 2) increased reaction rates. Decomposition gas generated within the impermeable pressed explosives could generate significant pressures leading to increased reaction rates and faster ignition times, even though the ullage is vented. Gas holdup within the pressed explosives may explain the anomalous ignition time for vented run 1.

Figure 4 shows a few of the temperature and pressure profiles from both the low-density (g) and high-density (23, 5, 7) SITI runs. Most of the measured pressures were smooth monotonically increasing functions as shown in Figure 4(a). Figure 4(a) also shows that the pressure history in the low-density SITI run g was similar to the pressure history in the large ullage run 26, which had similar boundary temperatures. Similar thermal ignition times for these two

experiments is likely due to similarity in temperatures and pressures.

The pressure-dependent kinetics were determined with the low-density molding powders to reduce issues associated with gases being retained within the explosive, which is common with the high-density PBX used in the current work. The density of the molding powder granules was about 1400 kg/m<sup>3</sup> with an effective spherical granule diameter of about 1 mm with 1050 granules per g [22]. At this density, the gas volume within the granules is 28 %, which may be open and connected to the gas volume between the granules as well as the extra gas volume or ullage. The pores within the granules can also be closed. In contrast, the density of the pressed PBX is about 1880 kg/m<sup>3</sup> with an internal gas volume of 3 %, which is usually assumed to be unconnected or closed.

Gas pressures are higher within the impermeable high-density PBX as decomposition gases accumulate during cookoff. After being exposed to high temperatures, the explosive may decompose into closed and unconnected pore volumes. Gaseous reaction rates increase in the closed pores due to the rapidly increasing internal pressures. Exothermic reaction rates begin to exhibit runaway behavior as energy generation exceeds conductive dissipation without a means to alleviate the increasing pressure.

Increasing temperature leads to thermal strain causing thermal damage where previously closed pores become connected and decomposition gases flow from the interior of the explosive into the gas ullage. Thermal damage is caused by a multitude of factors such as thermal expansion, crack formation, and material decomposition. Thermal damage causes an overall increase in measured pressure but a decrease in the internal gas pressure and subsequent lowering of the reaction rates. Thermal ignition in vented systems can be like thermal ignition in a sealed system if ther-

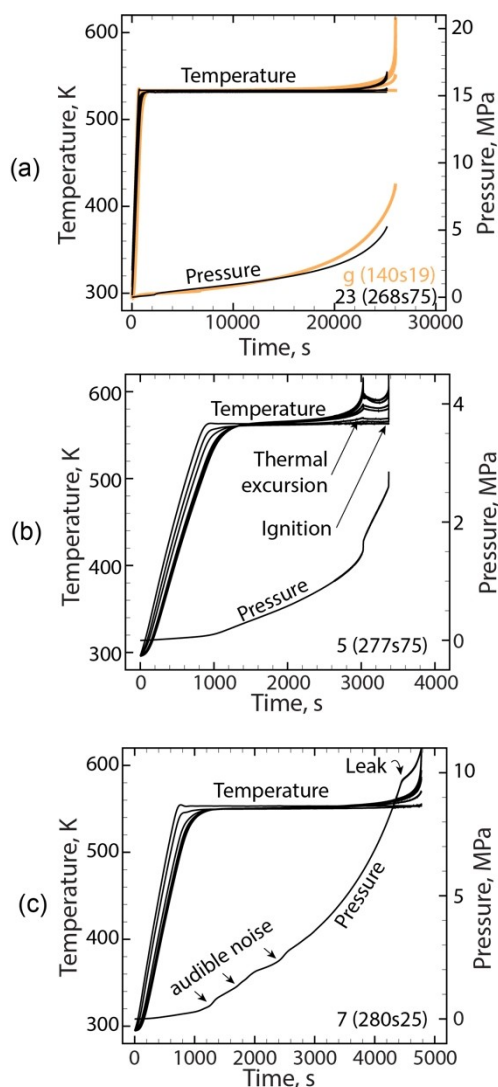


**Figure 4.** Measured temperatures and pressures from various SITI runs (a) g, 26, (b) 5, and (c) 7.

mal damage does not open the porosity in high-density explosives.

An example of thermal excursions causing thermal damage is shown in Figure 4(b) where a thermal excursion likely caused thermal damage, increased permeability, and an abrupt increase in the measured pressure. Although the measured pressure increases during the thermal excursion, the internal pressure is reduced, and the reaction rates slow down causing a decrease in the interior temperature of the PBX. Eventually, thermal runaway occurs as the overall pressure continues to increase. This phenomena, thermal ignition being postponed or arrested by thermal damage, is one explanation for the wide variability seen in ignition times for vented experiments with pressed PBX. Similar behavior is shown in Figure 4(c) as the pressed PBX cracks and

releases gas. Periodically, the release of gas is violent and is accompanied by audible noises (e.g., pop, crack, etc.).

## 2.2 Open SITI Tests

An open SITI experiment has been performed to visualize the dynamic thermal damage occurring to high-density vented PBX exposed to high temperatures. The open SITI experiment only considers the bottom half of the aluminum confinement with a single 2.54 diameter by 1.27 cm tall, pressed pellet. Figure 5(a) shows the boundary temperature of the confining aluminum and the top center surface of the PBX pellet for open run 283. Figures 5(b) shows two images of the initial pellet in the aluminum cup. The upper image in Figure 5(b) shows the explosive pellet before a large washer is installed to keep the pellet within the cup. Figures 5(c) shows several videos frames of these experiments.

Run 283 did not show significant volumetric strain or swelling as was observed in Figure 1(c). The first sign of damage for run 283 occurs abruptly at 5800 s as spall-like flakes of PBX were formed. At 5830 s, a large piece of the pellet was expelled from the camera view and yellow smoke evolved from the resulting hole. Eventually, the smoke cleared, and evidence of a conductive burn was observed as shown in the middle image of Figure 5(c). The difference between the damage shown in Figure 1(c) is related to the confinement with one being vented and the other being sealed with pressures approaching 10 MPa.

The right image in Figure 5(c) shows yellow crystals that formed as the residue cooled. Similar residue has

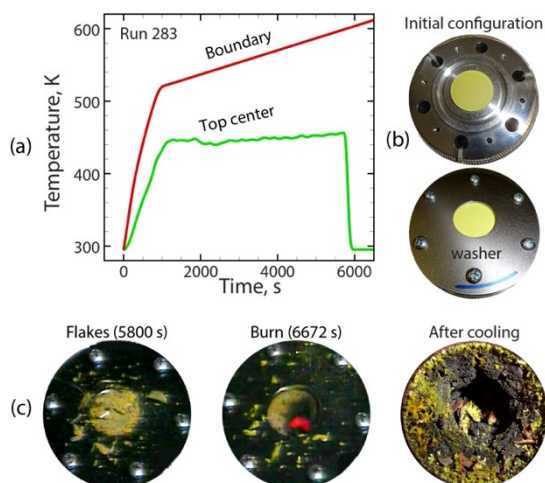


**Figure 5.** (a) Boundary and center temperatures in open SITI experiment 283 with only the bottom aluminum confinement and one of the explosive pellets. (b) Initial configuration with top showing pellet before installation of washer and bottom showing confining washer. (c) Damage showing flakes, burning, and crystallization after cooling.

been analyzed by Kahl et al. using various spectroscopic techniques. Kahl shows that the yellow residue has a lower energy content than TATB, with a loss of  $\text{-NO}_2$  and  $\text{-NH}_2$  features.

## 2.3 SITI Borescope Images

To better assess the damage occurring in sealed systems, we added a borescope camera to run 11. Figure 6 shows various images from this run along with the temperature and pressure profiles near the ignition. The borescope only had a single focal point.

Figure 6(a) shows a temperature excursion occurring before thermal ignition. The excursion in run 11 occurs at 7370 s. Image negatives at 7370 s show a white ring, which is the location of the explosive and aluminum interface. The dark circle in Figure 6(b) is the light reflection, which is black since the image is negative. At 7370.1 s, the image in Figure 6(c) shows a fragment of PBX, which spalled from the center of the light reflection. At 7370.4 s in Figure 6(d), there are small pieces of PBX on the surface of the explosive. This is similar to Figure 5(c) but occurs in the sealed system at about 2 MPa.

Figure 1(b,c) shows that the explosive can swell, without flake formation, as long as the ullage space is large. In contrast, Figures 5(c) and 6(c,d) show that the explosive can also create spall-like flakes and relieve internal pressure. These damage observations are the basis of the micro-mechanics (MMP) pressurization model discussed in the companion paper [1].

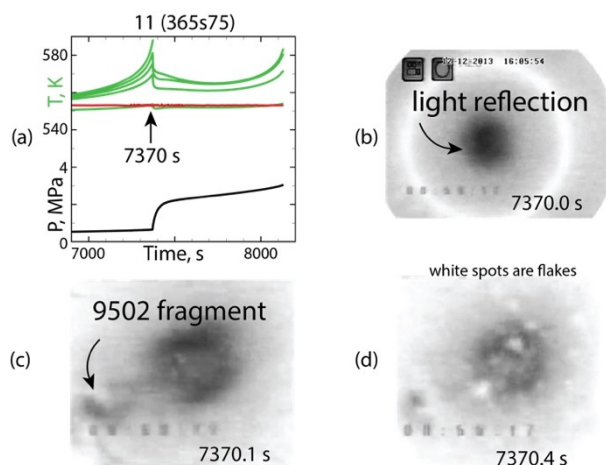


**Figure 6.** (a) Temperature and pressure plots for run 11. The green lines represent thermocouples 1, 3, 5, 7, and 9. The red line represents the boundary temperature of the aluminum, and the black lines represent the pressure in the ullage. (b,c,d) show borescope images at various times near the thermal excursion, showing damage that relieves internal pressure, but causes the measured ullage pressure to increase.

## 3 Model

We previously published [9,10] a pressure-dependent cook-off model calibrated using low-density molding powders of TATB PBXs. The pressurization model in [9] assumed that there was no bulk volumetric strain in the energetic material. Bulk volumetric strain is defined as the increase in overall explosive volume due to thermal expansion. No bulk volumetric strain implies that the initial volume remains unchanged, although the condensed volume was allowed to increase due to thermal expansion. The initial bulk explosive volume was maintained by decreasing the initial gas volume fraction causing internal porosity to decrease. The negligible bulk volumetric strain assumption is acceptable for low-density permeable explosives with large ullage space but not as accurate for high-density pressed PBXs that either swell with little mechanical damage or crack and release decomposition gases into the ullage space. In the current work, the negligible bulk strain assumption was replaced by the MMP model discussed in the companion paper [1]. In the current work, details of the kinetic model based on the universal cookoff model [2] are discussed in Section 3.1. The MMP model and parameters are discussed in [1].

### 3.1 Kinetic Model

The TATB reaction mechanism has been simplified by using a universal cookoff model (UCM) mechanism as described in [2]. The UCM uses four reaction pathways that represent 1) desorption of moisture, 2) a condensed-phase dominated reaction, 3) a gas-phase dominated reaction, and 4) a binder reaction. All four of the reaction rates use non-constant activation energies that are distributed with respect to the reaction progress. The gas-phase dominated reaction rate is accelerated by pressure using a  $(P/P_0)^n$  multiplier. The success of the UCM is attributed to the flexible form of the non-Arrhenius rate expressions. In the current work, we have combined the condensed-phase and gas-phase dominated reactions with no loss of accuracy. We also assume that the Kel-F binder is inert, which eliminates the need for the binder reaction. Thus, the UCM in the current paper uses two reactions: 1) moisture desorption and 2) TATB decomposition.

Table 3 provides the energy and species conservation equations, mechanism, and rate equations for the cookoff model. The nomenclature for this Table is given in Table 4. The conductive energy equation in Eq. (1) includes a volumetric source term,  $\sum_i h_{fi} r_i$ , to account for reaction enthalpy.

The stoichiometry for the TATB reaction was determined using the product hierarchy from an equilibrium calculation. The product hierarchy was assumed to be the same as the equilibrium composition at 400 K and 0.1 MPa. The product hierarchy does not change significantly at temper-

**Table 3.** TATB cookoff model.<sup>[a]</sup>

Energy	$\rho C_p \frac{\partial T}{\partial t} = \nabla \cdot (k \nabla T) + \sum_i h_i r_i$	(1)
Mechanism <sup>[b]</sup>	$M \xrightarrow{1} M_g; \text{TATB} \xrightarrow{2} 7.50 \text{ G} + 3.90 \text{ C}$	(2)
Rates	$r_1 = A_1 \exp\left(\frac{-E_1 + \zeta_1 \sigma_1}{RT}\right) [M]; r_2 = A_2 \left(\frac{P}{P_o}\right)^n T^m \exp\left(\frac{-E_2 + \zeta_2 \sigma_2}{RT}\right) [\text{TATB}]$	(3)
Species	$\frac{d[M]}{dt} = -r_1; \frac{d[M_g]}{dt} = r_1; \frac{d[\text{TATB}]}{dt} = -r_2; \frac{d[G]}{dt} = 7.50 r_2; \frac{d[C]}{dt} = 3.90 r_2$	(4)
Distribution <sup>[c]</sup>	$\xi_1 = \text{norminv}\left(\frac{[M]}{[M]_o}\right); \xi_2 = \text{norminv}\left(\frac{[\text{TATB}]}{[\text{TATB}]_o}\right)$	(5)

[a] Nomenclature and parameters are given in Table 4. [b] Equilibrium product hierarchy for reaction 2 is  $\text{TATB} \rightarrow 3 \text{ N}_2 + 2.4 \text{ H}_2\text{O} + 1.8 \text{ CO}_2 + 0.3 \text{ CH}_4 + 3.9 \text{ C}$ . [c] "norminv" is the inverse of the standard normal cumulative distribution. See Microsoft Excel function NORMINV.

ature and pressures near ignition states of 600 K and 40 MPa.

The thermodynamic pressure in Eq. (3),  $P$ , is determined using the MMP model [1]. Usually, a quasi-static mechanics equation is solved simultaneously with the energy equation to satisfy stress-strain relationships as discussed by Brown et al. [24]. However, in the current work, the thermodynamic pressure is determined by using an analytical solution for displacement caused by decomposition, thermal expansion, and internal and external pressure using the MMP model [1].

The thermophysical properties ( $C_p$  and  $k$ ) were taken from Lawless et al. [25] as well as Koerner et al. [26]. The rate coefficients ( $A_1$ ,  $E_1$ ,  $\sigma_1$ ) for the desorption reaction were taken from [9]. The initial amount of moisture,  $\omega_{M_r}$ , was taken from [27]. The reactive diffusion equations were solved in 1D using a multi-layer method-of-lines solver with stiff numerical methods and adaptive mesh refinement to resolve the steep temperature gradients associated with cookoff. More detail regarding the solution technique can be found in [28]. The SIT1 experiment has been modeled in both 1D and 2D axisymmetric geometries using both finite difference [28] and finite element solvers [29]. The results from both these solution techniques are similar since the ramp time is fast and the explosive reaches the set point temperature rapidly, even with large ullage experiments.

The rate coefficients for reaction (2) were determined by initially using the low-density vented SIT1 data run c (223v19) listed in Table 1. First, the activation energy and the distribution factor ( $E_2$  and  $\sigma_2$ ) were determined using the temperature profiles and ignition time by assuming  $m$  and  $n$  are zero. The activation energy ( $E_2$ ) was primarily determined with the ignition time, and the distribution parameter ( $\sigma_2$ ) was determined with the width of the temperature spread as the explosive starts to thermally run away. Large negative values of  $\sigma_2$  cause the temperature profiles to be compressed and smaller negative values (or positive values) of  $\sigma_2$  cause the temperature profiles to spread out. Negative values of  $\sigma_2$  cause the rate to accelerate. Positive values of  $\sigma_2$  cause the rate to decelerate.

Once the ignition times and temperature profiles were matched adequately, the ignition plot for the vented runs

was used to determine the pressure exponent,  $n$ , using the  $1000/T_{sp}$  vs time-to-ignition plot. Once  $n$  was determined with the sealed ignition plots. Some iteration of  $\sigma_2$  using run a (225s19) was required to match the pressure profile adequately. The steric factor,  $m$ , was determined using the slope of the  $1000/T_{sp}$  vs time-to-ignition plot. High positive values of  $m$  caused the ignition plot to rotate clockwise.

### 3.2 MMP Model Summary

The MMP model is based on pore growth at specified nucleation sites within the explosive. The pore radius increases as decomposition gases fill the pore. The pore radius also changes due to thermal expansion or compression. In the MMP model, the pore radius changes due to chemical reactions are determined separately from dimensional changes due to mechanics effects such as thermal expansion or compressibility. Details of the MMP model and parameters are given in a companion paper [1].

## 4 Results

The combined UCM/MMP cookoff model was applied to TATB-based PBXs with densities ranging from molding powders at 743 kg/m<sup>3</sup> (38%TMD) to high-density pressed explosives at 1904 kg/m<sup>3</sup> (98%TMD). Section 4.1 presents the SIT1 experiments that were run with both low-density and high-density explosives with various ullage volumes ranging from 25% to 75% of the overall confining volume. Section 4.2 contains predictions of the ODTX experiment from with densities ranging from 1652 kg/m<sup>3</sup> to 1904 kg/m<sup>3</sup>. Section 4.3 presents larger-scale predictions at 1890 kg/m<sup>3</sup> in the intermediate scale cookoff bucket (ISCB) tests [30].

### 4.1 SIT1 Predictions

The trend lines are shown in Figure 3(a) and (b) were predicted using the combined UCM/MMP model at 743 kg/m<sup>3</sup> and 1881 kg/m<sup>3</sup>, respectively. All predictions made in Fig-



**Table 4.** Nomenclature and model parameters.

Symbols	Description	Value	Units
$\ln(A_1), \ln(A_2)$	Natural logarithm of the pre-exponential factors	35, 35	$\ln(s^{-1})$
$[B]$	Inert binder concentration	$\omega_{\text{inert}} \times \rho_{\text{bo}} / M_{\text{wb}}$	$\text{kmol/m}^3$
$C, C_b$	Specific heat with linear interpolation and constant extrapolation [24,25]	SITI [24]: 1109 (300 K) and 2097 (700 K) ODTX [25]: 1100 (constant)	$\text{J kg}^{-1} \text{K}^{-1}$
$[C]$	Carbon concentration	Initially 0	$\text{kmol/m}^3$
$E_1/R, E_2/R$	Activation energy over $R$	25000, 15200	K
$\sigma_1/R, \sigma_2/R$	Standard deviation of activation energy over $R$	2500, -850	K
$[G_i]$	Gas concentration from TATB decomposition	Initially 0	$\text{kmol/m}^3$
$h_{fi} (i = M, M_{gr}, \text{TATB}, G, C)$	Heat for formation for $i^{\text{th}}$ species	$-285.8 \times 10^6, -241.8 \times 10^6, -145 \times 10^6, -174.8 \times 10^6, 0$	$\text{J/kmol}$
$h_{ri} (i = 1, 2)$	Heat of reaction for $i^{\text{th}}$ reaction	$h_{r1} = (h_{fMG} - h_{fM})$ $h_{r2} = (7.50h_{fG} + 3.9h_{fC} - h_{fTATB})$	$\text{J/kmol}$
$i$	$i^{\text{th}}$ species or $i^{\text{th}}$ reaction	$M, M_{gr}, \text{TATB}, G, C, \text{Kel-F}$ 1, 2	None
$k$	Thermal conductivity with linear interpolation and constant extrapolation [24,25].	SITI: 1881 $\text{kg/m}^3$ : 0.55 at 300 K SITI: 1881 $\text{kg/m}^3$ : 0.55 at 530 K SITI: 1881 $\text{kg/m}^3$ : 0.25 at 540 K SITI: 1881 $\text{kg/m}^3$ : 0.25 at $T > 540 \text{ K}$ SITI: 743 $\text{kg/m}^3$ : 0.14 (constant) ODTX [25]: 1904 $\text{kg/m}^3$ : 0.563 (constant) ODTX [25]: 1797 $\text{kg/m}^3$ : 0.500 (constant) ODTX [25]: 1652 $\text{kg/m}^3$ : 0.400 (constant)	$\text{W m}^{-1} \text{K}^{-1}$
$m$	Steric factor for reaction 2	-2.7	$\text{K}^{-1}$
$[M]$	Adsorbed moisture concentration	Initially $\omega_M \times \rho_{\text{bo}} / M_{\text{wM}}$	$\text{kmol/m}^3$
$[M_g]$	Desorbed moisture concentration	Initially 0	$\text{kmol/m}^3$
$M_{wi}$ where $i = M, M_{gr}, \text{TATB}, G, C, B$ (Kel-F)	Molecular weight of $i^{\text{th}}$ species	18.0, 18.0, 258.2, 28.2, 12, 413.3	$\text{kg kmol}^{-1}$
$n$	Pressure exponent	0.3	None
norminv	Inverse of the standard normal distribution	Function (see Microsoft Excel NORMINV)	None
$P$	Absolute pressure	Initially $P_o$	MPa
$P_o$	Initial pressure	0.083 (SITI in Albuquerque, NM) 0.101 (ODTX in Livermore, CA)	MPa
$P_{\text{fail}}$	Pore failure pressure	5	MPa
$\rho$	Density	Field variable	$\text{kg m}^{-3}$
$\rho_{\text{bo}}$	Initial bulk density	SITI: $743 \pm 3$ and $1881 \pm 5$	$\text{kg m}^{-3}$
$\rho_c$	Condensed density	Field variable	$\text{kg m}^{-3}$
$\rho_{\text{co}}$	Initial condensed density	1942	$\text{kg m}^{-3}$
$R$	Gas constant	8314	$\text{m}^3 \text{Pa K}^{-1} \text{kmol}^{-1}$
$S_f$	Solid fraction	$S_f = (Mw_M[M] + Mw_E[E] + Mw_C[C] + Mw_B[B]) / \rho_{\text{bo}}$	$\text{kg/kg}$
$t$	Time	Global variable	s
$T$	Temperature	Field variable	K
$[\text{TATB}]$	TATB concentration	Initially $\omega_{\text{TATB}} \times \rho_{\text{bo}} / M_{\text{wTATB}}$	$\text{kmol/m}^3$
$T_o$	Initial temperature	SITI experiments: $295.01 \pm 2.01$ ODTX experiments: 300 (assumed)	K
$V_{\text{ex}}$	Extra gas volume: $V_{\text{ex}} = V_{\text{tube}} + V_{\text{ullage}}$	$4.12 \times 10^{-6}$ (ave. for 25% ullage SITI runs) $12.98 \times 10^{-6}$ (ave. for 50% ullage SITI runs) $38.61 \times 10^{-6}$ (ave. for 75% ullage SITI runs)	$\text{m}^3$
$V_{\text{o,PBX}}$	Initial volume of explosive	SITI experiments: $12.87 \times 10^{-6}$ ODTX experiments: $1.07 \times 10^{-6}$	$\text{m}^3$
$V_{\text{tube}}$	Pressure tube volume	SITI experiments: $0.1-0.2 \times 10^{-6}$ ODTX experiments: none	$\text{m}^3$
$V_{\text{ullage}}$	Ullage volume	SITI experiments: $3.1 \times 10^{-6}-38.9 \times 10^{-6}$ ODTX experiments: $0.1 \times 10^{-6}$ (guess)	$\text{m}^3$
$\omega_M$	Mass fraction of adsorbed water [26]	0.002	$\text{kg/kg}$
$\omega_{\text{TATB}}$	Mass fraction of TATB	$0.095 \times (1 - \omega_M)$	$\text{kg/kg}$
$\omega_{\text{inert}}$	Mass fraction of Kel-F	$1 - \omega_M - \omega_{\text{TATB}}$	$\text{kg/kg}$
$\sigma_1$	norminv: inverse of the standard normal distribution	Field variable	None
$\sigma_1$	norminv for 1 <sup>st</sup> reaction	Field variable	None
$\sigma_2$	norminv for 2 <sup>nd</sup> reaction	Field variable	None

ure 3 were made assuming that the explosive was initially impermeable. The impermeable assumption for the molding powders implies that the spherical pores within the TATB crystals are isolated and closed and these pores do not open and connect until the pore pressure exceeds 5 MPa, the assumed pore failure pressure. More details regarding the pore failure pressure, which is an extrapolation

of compressive strength at elevated temperature are included in the companion paper [1]. The combined UCM/MMP model can also be run assuming that all pores are initially open. This is a good assumption for the low-density molding powders as shown in Figure 7.

Figure 7 shows a comparison between measured and predicted ignition times for the low-density PBX experi-

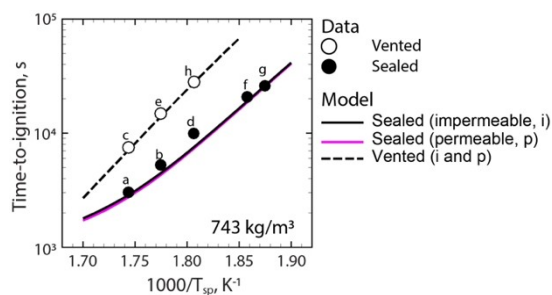


**Figure 7.** Predicted (lines) and measured (symbols) thermal ignition times for the molding powders at 743 kg/m<sup>3</sup> listed in Table 1 showing the insignificance of the initial permeability assumption for powders.

ments listed in Table 1. The UCM/MMP model predictions in Figure 7 were made using two separate assumptions regarding the initial permeability: 1) the explosive is permeable to the decomposition gases (pink line) and 2) the explosive is initially impermeable to the decomposition gases (black line). The predicted ignition times represented by the pink line are slightly lower than predictions represented by the black line.

Figures 8(a) and 8(b) show measured and predicted internal temperatures for vented SITI run c (223v19) and sealed SITI run a (225s19), respectively. The measured and predicted pressures are also shown in Figure 8(b). In Figure 8(b), the UCM/MMP model was run by assuming the initial porosity was impermeable (black dashed lines) or permeable (pink dashed lines). Both models match the measured ignition time, but the pressure prediction using the impermeable assumption matched the pressure profile better. Both predictions are adequate and the better predictions using the impermeable assumption may be fortuitous since this model option was used during the fitting of the rate coefficients.

UCM/MMP model predictions include the field variables temperature ( $T$ ), the solid fraction ( $S_s$ ), gas volume fraction ( $\phi$ ), pressure ( $P$ ), pore metrics (radius “ $a$ ” and half the distance between pores, “ $b$ ”), volumetric strain, gas molecular weight, and specific surface area. Global or averaged variables are predicted in the permeable layers. Predictions of the field variables for run a (225s19) are presented in Figures 9 and 10. Predictions of the global variables for run a (225s19) are given in Figure 11. The predictions in Figures 9–11 were made by assuming the explosive was initially impermeable. Similar predictions were given for the high-density SITI run 7 (280s25) in the companion paper [1].

Figure 9 shows the temperature, solid fraction, gas volume fraction, and pressure as a function of the radial distance and time for run a (225s19) which was ramped from room temperature to 573.51 s in 700 s and then held at 573.51 seconds. Most of the predictions in Figures 9 and 10 are only for the explosive and not the confining aluminum, except for Figure 9(a) which shows the temperature in part

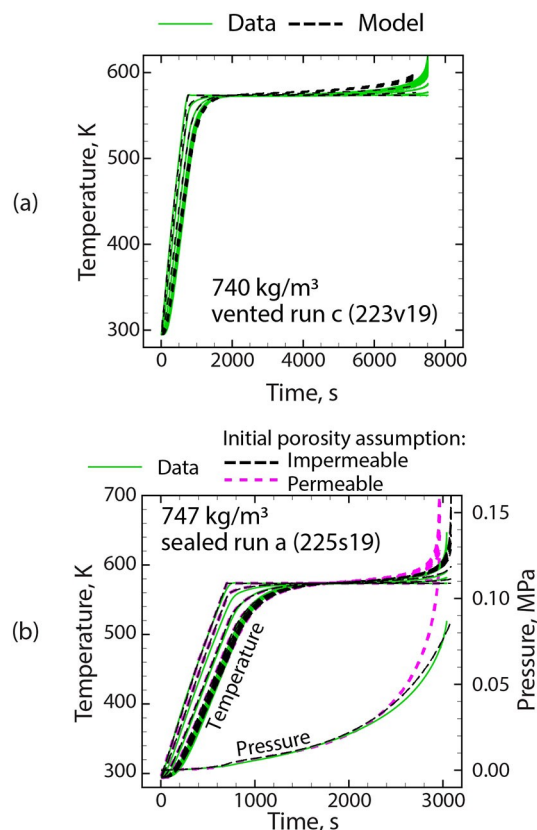


**Figure 8.** Predicted (black dashed lines) and measured internal temperature (green lines) from SITI (a) run c and (b) run a. The temperatures are located at the radial locations given in Figure 2(b). The measured (green line) and predicted pressure in the ullage assuming the initial porosity was either closed (black dashed lines) or open (pink dashed lines) are given in (b).

of the confining aluminum. Thermal ignition occurs in the center of the explosive where temperatures rapidly increase simultaneously with a decrease in the solid fraction and an increase in the gas volume fraction ( $\phi$ ) and pressure ( $P$ ) as shown in Figures 9(b) and (c), respectively.

At the pore failure pressure (5 MPa), the pores transition from being closed to open as shown in Figure 9(c). This transition is better depicted in Figure 9(d) which shows pressure every 5 s along with the radial distance. The explosive starts to transition from having all closed pores to open pores starting at a radial distance between 0 and 1.8 mm from 3010 to 3015 seconds. Once the pores open, the gases combine with the other gases in open pores as well as the external ullage. The pressure gradient between the pores disappears as the pores open and the gases mix.

Figure 10 shows how the morphology changes during decomposition. Figure 10(a) shows the changing pore radius in response to changing temperature and reaction. “ $a$ ” in Figure 10(a) represents the pore radius and “ $b$ ” in Figure 10 (a) represents half the average distance between pores as shown in the inset in Figure 10(a). Figure 10(b) shows the

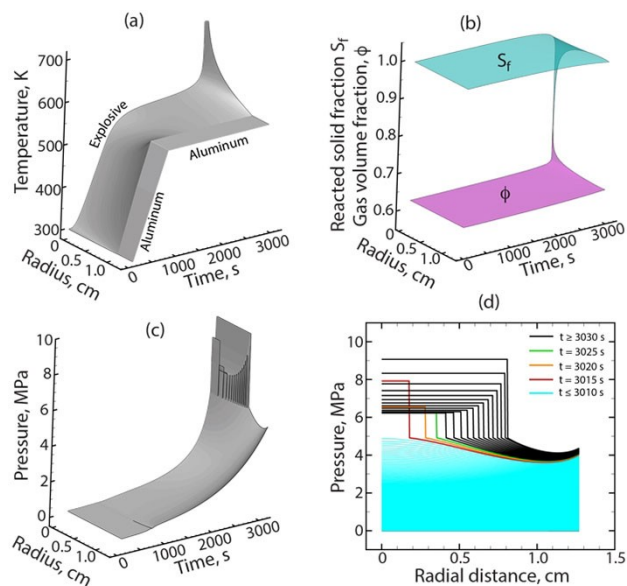


**Figure 9.** Predicted (a) temperature, (b) solid fraction, gas volume fraction, (c,d) pressure for SITI run a (225s19).

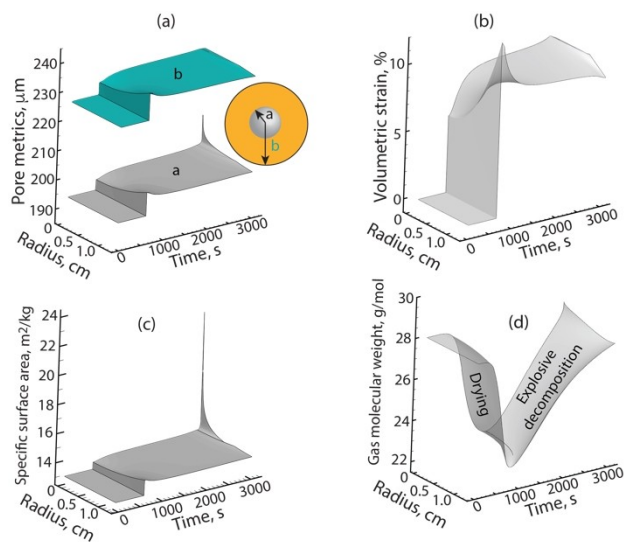


**Figure 10.** Predicted (a) pore metrics, (b) volumetric strain, (c) specific surface area, and (d) gas molecular weight. The pore metrics include the pore radius,  $a$ , and half the distance between pores,  $b$ , as shown in the inset in (a). The volumetric strain is  $\varepsilon = (b/b_0)^3 - 1$ .

percent volumetric strain,  $\varepsilon = (b/b_0)^3 - 1$ . Figure 10(c) presents the predicted specific surface area, which increases from about 12 to 24 m<sup>2</sup>/kg.

Figure 10(d) presents the average gas molecular weight within the pores. Initially, the pore gas is assumed to be air with a molecular weight of 28 g/mol. As the explosive temperature increases, moisture is evolved and mixes with the air, and the average molecular weight decreases. As the explosive heats further, the explosive decomposes into gas

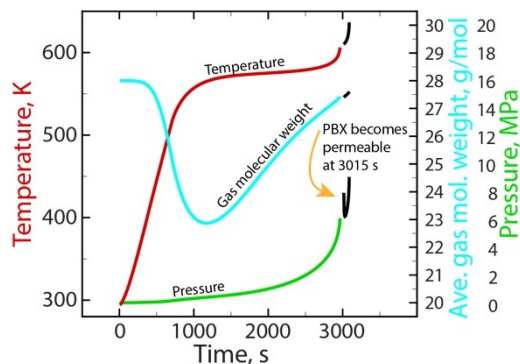


**Figure 11.** Predicted temperature, gas molecular weight, and pressure within the permeable regions of run a (225s19). The predictions displayed as colored lines (red, cyan, and green) were made by assuming that the initial explosive was completely permeable to decomposition gases. The predictions displayed as black lines were made by assuming that the initial explosive was impermeable to decomposition gases. The explosive only became permeable after the pore pressure exceeded 5 MPa. This occurs at 3015 s as highlighted with the orange arrow.

with a molecular weight of 28.2 g/mol, which mixes with the pore gases.

Figure 11 shows predictions of the average gas temperature, pressure, and molecular weight as calculated with the following equations from [1]:

$$\tilde{P}_r = \frac{\tilde{z}_r \tilde{\rho}_r \tilde{R} \tilde{T}_p}{\tilde{Mw}_p} \quad (6)$$

$$\tilde{T}_p = \frac{\int_{\text{permeable}} \phi_r T dV}{\int_{\text{permeable}} \phi_r dV} \quad (7)$$

$$\tilde{Mw}_p = \frac{\int_{\text{permeable}} \phi_r Mw_g dV}{\int_{\text{permeable}} \phi_r dV} \quad (8)$$

The colored lines in Figure 11 are for predictions made by assuming that the initial explosive was permeable to decomposition gases. The black lines in Figure 11 are for predictions made by assuming that the initial explosive was impermeable to decomposition gases. Gases do not mix with the permeable parts of the explosive until the pore pressure exceeds 5 MPa. This did not occur until 3015 s as annotated in Figure 11.

## 4.2 ODTX Predictions

The Lawrence Livermore National Laboratory's one-dimensional time-to explosion (ODTX) experiment confines a 1.27 cm diameter sphere of the TATB-based PBX between two 7.62 cm diameter aluminum cylinders using a hydraulic press [26]. The two aluminum cylinders each have a 1.27 cm

diameter hemisphere machined into the end faces of the cylinders. A knife edge groove is also machined around the circumference of the hemispheres. The explosive is placed in the hemispherical cavity as the aluminum cylinders are pressed together to deform a copper O-ring that confines the PBX. The hydraulic pressure holding the two aluminum cylinders together is 151.7 MPa. The aluminum cylinders are preheated to a set point temperature. The ODTX experiment has a constant temperature boundary.

Koerner et al. [26] studied three densities of TATB-based PBXs: 1652 kg/m<sup>3</sup> (85% TMD), 1797 kg/m<sup>3</sup> (92.5% TMD), and 1904 kg/m<sup>3</sup> (98% TMD). Figure 12 shows the measured (symbols) and predicted (lines) time-to-explosions for these experiments. All the predictions in Figure 12 were made using a constant specific heat ( $C_p$ ) and thermal conductivity ( $k$ ) as suggested by Koerner et al. [26]. The specific heat was 1100 J kg<sup>-1</sup> K<sup>-1</sup> (all densities) and thermal conductivities were 0.4, 0.5, and 0.6 W m<sup>-1</sup> K<sup>-1</sup> for the 85%, 92.5%, and 98% TMD PBX, respectively. The experiments that were sealed are represented by solid circles. The experiments that were vented are represented by open circles. The vented experiments did not use the copper O-ring to confine the gases. Similar ignition times for confined and unconfined ODTX may be caused by gas retention within closed pores even without an O-ring seal.

Figure 12 shows predicted thermal ignition times as orange lines. Thermal ignition occurs when the heat generated by a chemical reaction exceeds the heat dissipation rate, which is typically limited by thermal conduction. Evi-

dence of thermal ignition are temperature excursions as shown in Figure 8 or Figure 9(a). Sometimes the confining vessel will fail before thermal runaway is obtained. Failure of the container due to increased pressure is referred to in the current work as a pressure breach. In Figure 12, the blue lines represent the time that the confining hydraulic pressure is exceeded which is equivalent to a pressure breach.

Both the calculated time of the thermal ignition and the pressure burst in Figure 12(b) and Figure 12(c) match the measured time-to-explosion. However, for the high-density explosives in Figure 12(a), the measured time-to-explosion is bound by the calculated thermal ignition time and the pressure burst time.

### 4.3 ISCB Predictions

Parker et al. [30] provided a set of cookoff experiments at larger scales for model validation. Each intermediate-scale cookoff bucket test (ISCB) consisted of two stacked 7.62 cm diameter by 7.62 cm tall cylinders of the TATB-based PBX pressed to 1890 kg/m<sup>3</sup> as shown in Figure 13(a) for a combined mass of 1.3 kg of explosive. The thickness of the confining aluminum wall was nominally 1.27 cm. The ISCB experiment was heated radially using band heaters controlled

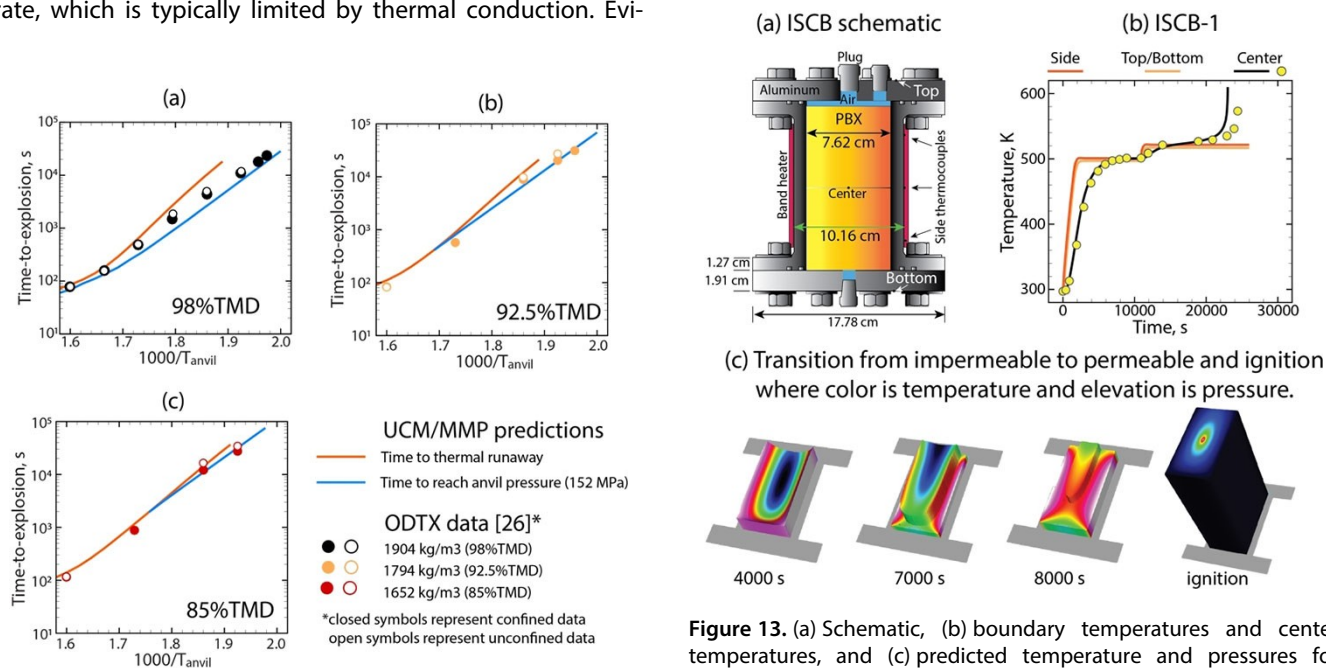


**Figure 12.** Predicted (lines) and measured (symbols) representing time-to-explosion as a function of the inverse of the anvil temperature. The orange lines are predicted thermal ignition times. The blue lines are predicted pressure burst times. The closed symbols were sealed using deformable copper gaskets. The open symbols were not sealed.

**Figure 13.** (a) Schematic, (b) boundary temperatures and center temperatures, and (c) predicted temperature and pressures for ISCB-1. In (c), dark blue represents the coldest temperature, and white/pink represents the hottest temperature. The pressure in (c) is represented by the height of the explosive above the midplane with the pressure being 150 MPa at ignition. The symbols in (b) represent measured center temperatures from [30]. The colored lines in (b) were used as boundary temperatures and the black line is the predicted center temperature.



by a thermocouple on the outside of the aluminum bucket. The proposed thermal profile was to heat to 503 K and soak for 2.5 h, then raise to either 523 K or 543 K and hold until thermal runaway.

Thermocouples were placed between the two cylinders, as well as on the exterior, top, and bottom of the aluminum confinement. The temperature along the side of the confinement is shown in Figure 13(b) and is the average of the three side thermocouples shown in the schematic of Figure 13(a). The top and bottom temperatures of the ISCB-1 test were nearly the same as shown in Figure 13(b). The predicted (black line) and measured (yellow circles) represent the center temperature between the two cylinders labeled as "Center" in Figure 13(a).

Figure 13(c) presents predictions of both temperature and pressure at 4000 s, 7000 s, 8000 s, and at ignition. The color scale changes from image to image with the maximum temperature corresponding to pink and the coolest temperature corresponding to blue. The pressure is represented by the height of the surface above the center plane of the ISCB experiment. At 4000 s the explosive is impermeable and spatial pressure gradients are shown in Figure 13(c). As the pore pressure reaches 5 MPa, the pore transitions from a closed pore, impermeable explosive, to an open pore permeable explosive. The transition is complete before the second temperature plateau is imposed. Thermal ignition was predicted to occur at 23015 s which is 5.6% less than the measured ignition time of 24383 s.

## 5 Uncertainty Analysis

In the companion paper [1], an uncertainty analysis was performed on SITI run 7 (280s25) where only uncertainty in

the mechanical parameters was investigated. Only the pore failure pressure contributed significantly to the uncertainty in the predicted ignition times for run 7. In the current paper, run 4 (252s25) is performed using the uncertainty associated with thermal, chemical, and mechanical parameters.

Uncertainty in model response caused by uncertainty in model parameters is determined using a Latin Hypercube Sample (LHS) analysis [31]. LHS analysis is a smart Monte-Carlo uncertainty technique wherein the probability of choosing a random input parameter in the tails of the distribution has the same probability of choosing an input parameter near the mean of the distribution. In the current work, the distributions were assumed to be uniform.

Table 5 presents fifteen input parameters along with the range of uncertainty in these parameters. Twenty sets of the 15 parameters were determined using LHS sampling techniques [31]. Predictions from the twenty sets of input parameters are shown in Figure 14(a). Ignition times were determined using these 20 sets for input parameters. The Pearson correlation coefficient [32] between the input parameters and predicted ignition times are listed in Table 5 and represented by  $r$ .

Figure 14(a) shows the uncertainty in the predicted temperature (dark blue lines) and pressure (black line) profiles for run 4 (252s25). These predictions are of the average temperature and pressure within the ullage. The measured pressure in the ullage is represented by the green line in Figure 14(a). The external boundary temperature (red line) and the center temperature (cyan line) are also shown in Figure 14(a).

The only parameter contributing significantly to the uncertainty in the predicted ignition times for run 4 (252s25) was the extra gas volume associated with the ullage and pressure tubing leading to the pressure transducer,  $V_{ex}$ . For

**Table 5.** MMP model parameter uncertainty and correlation coefficient between the parameter and the ignition time for run 4 (252s25).<sup>[a]</sup>

Symbol		Description	Range <sup>[b]</sup>	r
1	b <sub>o</sub>	Initial outer radius, μm	100–352	−0.05
2	β <sub>mult</sub>	Vol. exp. coef. multiplier	0.9–1.1	0.06
3	C <sub>300</sub>	Specific heat at 300 K	1054–1164	−0.05
4	C <sub>700</sub>	Specific heat at 700 K	1992–2202	0.00
5	k <sub>530</sub>	Thermal conductivity at 530 K	0.5–0.6	−0.05
6	k <sub>540</sub>	Thermal conductivity at 540 K	0.2–0.3	−0.06
7	P <sub>fail</sub>	Failure pressure, MPa	1–9	−0.03
8	ρ <sub>bo</sub>	Initial bulk density, kg/m <sup>3</sup>	1871–1891	0.05
9	S <sub>L</sub>	Longitudinal sound speed, m/s	2466–3014	0.05
10	S <sub>s</sub>	Shear sound speed, m/s	1242–1518	0.03
11	T <sub>o</sub>	Initial temperature, K	290–300	0.08
12	U <sub>r1</sub>	Reaction rate 1 multiplier	0.9–1.1	0.08
13	U <sub>r2</sub>	Reaction rate 2 multiplier	0.9–1.1	−0.04
14	V <sub>ex</sub>	Extra gas vol. (Vullage + Vtube), cm3	4.00–4.94	0.99
15	ω <sub>S</sub>	Initial moisture mass fraction	0.001–0.003	0.06

[a] The ignition time determined with the 20 LHS samples was  $2752 \pm 48$  s (mean  $\pm$  1 st.dev). The measured ignition time for run 4 (252s25) was 2636 s giving a +4% error. [b] The range of the parameters is assumed to have a uniform distribution about the mean. The uncertainty range in  $E$ ,  $k$ , and  $v$  are estimated based on uncertainty in the longitudinal sound speed and the shear sound speed so that  $E$ ,  $k$ , and  $v$  are consistent for each LHS sample.

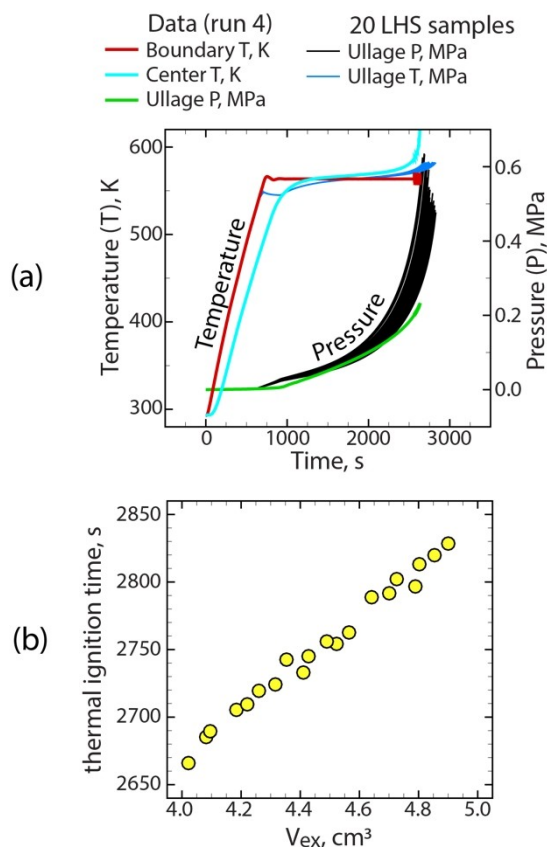


**Figure 14.** (a) Measured boundary temperature (red line), center temperature (cyan line), and ullage pressure (green line). LHS predictions of ullage pressure (black lines) and ullage temperature (dark blue lines). (b) Variation of predicted ignition time with the extra volume associated with the ullage and tubing volume.

this parameter, the correlation coefficient was 0.99 as shown in Table 5. Figure 14(b) also shows the strong correlation between the predicted ignition times and  $V_{ex}$ .

In the uncertainty analysis in the companion paper, the error between the predicted and measured ignition times for run 7 was  $-3\%$  with most of the uncertainty associated with the pore failure pressure. The error for the predicted ignition times in the current paper for run 4 was  $+4\%$  with most of the uncertainty associated with the extra volume.

## 6 Summary and Conclusions

The current paper is a companion paper to [1], which describes a micromechanics pressurization (MMP) model for the cookoff of explosives. The MMP model is coupled to a universal cookoff model (UCM) that supplies temperature and decomposition chemistry to the MMP model which determines pressure. The current paper primarily describes the thermal chemistry (UCM model) and the coupling between the UCM model and the MMP model.

The coupled model is referred to as the UCM/MMP model. The UCM/MMP model predicts ignition time as well as spatially dependent field variables such as temperature, pressure, solid fraction, gas volume fraction, and gas molecular weight. Example calculations are given in the paper for these field variables for the low-density molding powders. Similar predictions were made in the companion paper [1] for high-density PBX. The UCM/MMP model also predicts the damage state of the explosive such as pore size, volumetric strain, and specific surface area. In the current paper, the UCM/MMP model is applied to the cookoff of both powdered and pressed explosive.

The UCM/MMP model uses a simple two-step reaction mechanism that describes desorption of moisture and decomposition of TATB into equilibrium products. The UCM model solves the conductive energy equation with a volumetric source for decomposition chemistry. The UCM model predicts the composition of the evolving decomposition gases and provides the MMP model with the solid fraction, which is used to determine the change in pore radius due to reaction. The MMP model uses a gas equation of state in conjunction with the evolving molecular weight, gas density, volumetric thermal expansion, and compressibility to determine the pore pressure. Pressure couples the MMP model with the UCM model since the explosive decomposition rate is pressure dependent.

The UCM/MMP model can be run using two separate assumptions regarding the state of the pores within either pristine or mechanically damaged explosives. The initial explosive can be either impermeable to decomposition gases with the pores being closed or permeable to decomposition gases with the pores being open. Any combination of permeable and impermeable layers can be used to represent mechanically damaged explosive. The impermeable assumption in powdered explosives refers to the region within individual crystals rather than between the interstitial volume between the prills. For low-density explosives, the UCM/MMP model gives similar results for ignition times for both assumptions regarding permeability.

The kinetics for the UCM model was fit with the low-density molding powders by assuming the prills were initially impermeable to the decomposition products that accumulate within the TATB crystals. The model was used to predict thermal ignition in the SIT1 experiments for temperatures ranging between 526 K and 588 K for both the low-density explosive at  $743 \text{ kg/m}^3$  (38% TMD) and high-density explosive at  $1881 \text{ kg/m}^3$  (97% TMD). The model was also validated with ODTX data at three densities of  $1652 \text{ kg/m}^3$  (85% TMD),  $1797 \text{ kg/m}^3$  (92.5% TMD), and  $1904 \text{ kg/m}^3$  (98% TMD). A final validation prediction of the ignition time of 1.3 kg of explosive in the ISCB experiment. The difference between the predicted and measured ignition time for the ISCB experiment was 5.6%.

An LHS sensitivity analysis was performed on a single high-density SIT1 experiment. A similar sensitivity analysis was done on a different high-density SIT1 experiment in the

companion study [1]. The error between the measured and mean predicted ignition times for these two runs were  $-3\%$  and  $+4\%$ , respectively. Future work should consider validating the UCM/MMP model with mesoscale simulations using a fully coupled thermal, chemical, and mechanics solution. Future experiments should also consider larger-scale experiments with mechanically induced damage.

## Acknowledgements

Sandia National Laboratories is a multimission laboratory managed and operated by National Technology & Engineering Solutions of Sandia, LLC, a wholly owned subsidiary of Honeywell International Inc., for the U.S. Department of Energy's National Nuclear Security Administration under contract DE-NA0003525. This paper describes objective technical results and analysis. Any subjective views or opinions that might be expressed in the paper do not necessarily represent the views of the U.S. Department of Energy or the United States Government. We would like to thank Shane Snedigar for running the SIT1 experiments, Bill Erikson, Kevin Long, Sean Maharrey, and Tyler Voskuilen for internal review.

## Data Availability Statement

Research data are not shared.

## References

- [1] M. L. Hobbs, J. A. Brown, M. L. Kaneshige, C. Aviles-Ramos, A micromechanics pressurization model for cookoff, *Propellants Explos. Pyrotech.* **2021**, 46. DOI: 10.1002/prep.202100155.
- [2] M. L. Hobbs, M. J. Kaneshige, W. W. Erikson, A universal cookoff model for explosives, 50th International Annual Conference of the Fraunhofer ICT, Energetic Materials – Past, Present, and Future, June 25–28, **2019**, Karlsruhe, Germany.
- [3] C. L. Armstrong, J. T. Mang, Thermally-Driven Changes to Porosity in TATB-Based High Explosives, *Propellants Explos. Pyrotech.* **2021**, 46, 1304–1312.
- [4] J. C. Dallman, J. Wackerle, Temperature-dependent shock initiation of TATB-based high explosives, Tenth Symposium (International) on Detonation, July 21–16, **1993**, Boston, MA, USA, 130–138.
- [5] P. A. Urtiew, J. L. Cook, J. L. Maienschein, C. M. Tarver, Shock sensitivity of IHE at elevated temperatures, Tenth Symposium (International) on Detonation, July 21–16, **1993**, Boston, MA, USA, 139–147.
- [6] R. R. McGuire, C. M. Tarver, Chemical decomposition models for the thermal explosion of confined HMX, TATB, RDX, and TNT explosives, Seventh Symposium (International) on Detonation, June 16–19, 1981, Annapolis, MA, USA, 56–64.
- [7] C. M. Tarver, J. G. Koerner, Effects of endothermic binders on times to explosion of HMX- and TATB-based plastic bonded explosives, *J. Energ. Mater.* **2008**, 26, 56. DOI: 10.1080/07370650701719170.
- [8] M. A. Englert-Erikson, M. D. Holmes, G. R. Parker, C. C. Schmidt, B. A. Meyer, Gas transport in the insensitive high explosive PBX 9502, *Propellants Explos. Pyrotech.* **2020**, 45, 850. DOI: 10.1002/prep.201900337.
- [9] M. L. Hobbs, M. J. Kaneshige, Ignition experiments and models of a plastic bonded explosive (PBX 9502), *J. Chem. Phys.* **2014**, 140, 124203. DOI: 10.1063/1.4869351.
- [10] C. Aviles-Ramos, M. L. Hobbs, G. R. Parker, M. J. Kaneshige, M. J. Holmes, Validation of a Pressure Dependent PBX 9502 Cookoff Model, 15th International Detonation Symposium, July 13–18, **2014**, San Francisco, CA, USA, 711–720.
- [11] J. S. Moore, M. A. McClelland, P. C. Hsu, G. F. Ellsworth, E. M. Kahl, H. K. Springer, Thermal safety modeling of TATB-based explosive, 16th International Detonation Symposium, July 15–20, **2018**, Cambridge, MD, USA, 936–945.
- [12] W. W. Erikson, M. J. Martinez, M. L. Hobbs, M. J. Kaneshige, A. B. Dodd, Modeling explosive decomposition and cookoff with the porous flow, JANNAF 23rd PSHS Joint Meeting, San Diego, CA, USA **2006**, p. 1–10.
- [13] M. L. Hobbs, M. J. Kaneshige, Small-scale cook-off experiments and models of ammonium nitrate, *J. Energ. Mater.* **2018**, 37, 29. DOI: 10.1080/07370652.2018.1521480.
- [14] M. L. Hobbs, M. J. Kaneshige, D. W. Gilbert, S. K. Marley, S. N. Todd, Modeling TNT Ignition, *J. Phys. Chem. A* **2009**, 113, 10474. DOI: 10.1021/jp906134f.
- [15] M. L. Hobbs, W. B. Wente, M. J. Kaneshige, PETN Ignition Experiments and Models, *J. Phys. Chem. A* **2010**, 114, 5306. DOI: 10.1021/jp1007329.
- [16] M. L. Hobbs, M. J. Kaneshige, W. W. Erikson, Modeling the measured effect of a nitroplasticizer (BDNPA/F) on cookoff of a plastic bonded explosive (PBX 9501), *Combust. Flame* **2016**, 173, 132–150. DOI: 10.1016/j.combustflame.2016.08.014.
- [17] M. L. Hobbs, M. J. Kaneshige, W. W. Erikson, K. T. Miers, Gas retention in an HMX-based explosive (LX-14), *Sci. Tech. Energetic Materials* **2018**, 79, 35.
- [18] M. L. Hobbs, M. J. Kaneshige, C. D. Yarrington, Large deformation and gas retention during cookoff of a plastic bonded explosive (PBX 9407), *Combust. Flame* **2018**, 198, 278. DOI: 10.1016/j.combustflame.2018.09.020.
- [19] M. L. Hobbs, M. J. Kaneshige, W. W. Erikson, J. A. Brown, M. U. Anderson, S. N. Todd, D. G. Moore, Cookoff modeling of a melt cast explosive (Comp-B), *Combust. Flame* **2020**, 215, 36. DOI: 10.1016/j.combustflame.2020.01.022.
- [20] M. L. Hobbs, M. J. Kaneshige, S. Coronel, Vented and sealed cookoff of powdered and pressed  $\epsilon$ -CL-20, *J. Energ. Mater.* **2020**, 1, 1–20. DOI: 10.1080/07370652.2020.1814448.
- [21] M. L. Hobbs, M. J. Kaneshige, Cookoff of Black Powder and Smokeless Powder, *Propellants Explos. Pyrotech.* **2021**, 46, 484. DOI: 10.1002/prep.202000214.
- [22] B. Olinger, Compacting plastic-bonded explosive molding powders to dense solids, Report LA-14173, Los Alamos National Laboratory, Los Alamos, NM, USA **2005**.
- [23] E. M. Kahl, N. K. Muetterties, A. J. Nelson, H. E. Mason, J. V. Crowhurst, K. R. Coffee, J. S. Moore, J. G. Reynolds, Characterization of Solid Residue Formation in LX-17 Exposed to Abnormal Thermal Environments, 21st Biennial Conference of the APS Topical Group on Shock Compression of Condensed Matter, Portland, OR, USA, **2019**. DOI: 10.1063/12.0000948.
- [24] J. A. Brown, M. A. Cooper, W. W. Erikson, M. L. Hobbs, M. J. Kaneshige, Thermal ignition of mechanically damaged energetic materials, JANNAF 32nd Energetic Systems Hazards Joint Subcommittee Meeting, Virtual, December 7–17 **2020**.
- [25] Z. D. Lawless, M. L. Hobbs, M. J. Kaneshige, Thermal conductivity of energetic materials, *J. Energ. Mater.* **2019**, 38, 214. DOI: 10.1080/07370652.2019.1679285.
- [26] J. Koerner, J. Maienschein, B. Alan, A. Wemhoff, ODTX Measurements and Simulations on Ultra Fine TATB and PBX-9502,

- North American Thermal Analysis Society 35th Annual Conference, Aug. 26–29, **2007**, East Lansing, MI, USA.
- [27] E. A. Glascoe, L. N. Dinh, W. Small, G. E. Overturf, Moisture Desorption Rates from TATB Formulations: Experiments and Kinetics Models, *J. Phys. Chem. A*. **2012**, *116*, 5312. DOI: 10.1021/jp303074 g.
- [28] R. J. Gross, M. R. Baer, M. L. Hobbs, XCHEM-1D A Heat Transfer/Chemical Kinetics Computer Program for Multilayered Reactive Materials, Report SAND93-1603, Sandia National Laboratories, Albuquerque, NM, USA **1993**.
- [29] S. T. D. Team, SIERRA Multimechanics Module: Aria User Manual – Version 4.58, Report SAND2020-11537, Sandia National Laboratories, Albuquerque, NM, USA **2020**.
- [30] G. R. Parker, M. D. Holmes, P. Dickson, The Effect of Pressure and Venting on the Slow Cookoff of PBX 9502 in the Intermediate-scale Bucket Test, Report LA-UR-13-25716, Los Alamos National Laboratory, Los Alamos, NM, USA **2013**.
- [31] M. D. McKay, R. J. Beckman, W. J. Conover, A Comparison of three methods selecting values of input variables in the analysis of output from a computer code, *Technomet* **1979**, *21*, 239. DOI: 10.2307/1268522.
- [32] J. L. Rodgers, W. A. Nicewander, Thirteen ways to look at the correlation coefficient, *Am. Stat.* **1988**, *42*, 59. DOI: 10.1080/00031305.1988.10475524.

Manuscript received: May 26, 2021

Revised manuscript received: September 8, 2021

Version of record online: November 15, 2021